Field- Aligned Low-Energy O+ Flux Enhancements in the Inner Magnetosphere Observed by Arase

doi: https://doi.org/10.1029/2021JA029168

JGR Space Physics

RESEARCH ARTICLE
10.1029/2021JA029168

Special Section:
Geospace multi-point observations in Van Allen Probes and Arase era

Field-Aligned Low-Energy O^+ Flux Enhancements in the Inner Magnetosphere Observed by Arase

M. Nosé[1], A. Matsuoka[2], Y. Miyoshi[1], K. Asamura[3], T. Hori[1], M. Teramoto[4], I. Shinohara[3], and M. Hirahara[1]

[1]Institute for Space-Earth Environmental Research, Nagoya University, Nagoya, Japan, [2]Graduate School of Science, Kyoto University, Kyoto, Japan, [3]Institute of Space and Astronautical Science, Japan Aerospace Exploration Agency, Sagamihara, Japan, [4]Department of Space Systems Engineering, Kyushu Institute of Technology, Kitakyusyu, Japan

Key Points:

- O^+ flux enhancements that have energy-dispersed signatures at <~5 keV appear a few minutes after magnetic field dipolarization
- The lowest energy of ~10 eV and a field-aligned distribution of the O^+ flux enhancements suggest prompt extraction from the ionosphere
- The field-aligned low-energy O^+ flux enhancements can be a source of the warm plasma cloak

Citation:
Nosé, M., Matsuoka, A., Miyoshi, Y., Asamura, K., Hori, T., Teramoto, M., et al. (2021). Field-aligned low-energy O^+ flux enhancements in the inner magnetosphere observed by Arase. *Journal of Geophysical Research: Space Physics*, *126*, e2021JA029168. https://doi.org/10.1029/2021JA029168

Received 22 JAN 2021
Accepted 8 JUL 2021

Abstract The present study examines the low-energy ion flux variations observed by the Arase satellite in the inner magnetosphere. From the magnetic field and ion flux data obtained by the fluxgate magnetometer and the low-energy particle experiments–ion mass analyzer onboard Arase, we find 55 events of the low-energy O^+ flux enhancement accompanied with magnetic field dipolarization in the periods of April 1–October 31, 2017 and July 1, 2018–January 31, 2019. The low-energy O^+ flux enhancements (a) start a few minutes after the dipolarization onset, (b) have energy-dispersed signatures with decreasing energy from a few keV down to ~10 eV, (c) are observed in both storm and non-storm periods, (d) have a field-aligned distribution ($\alpha \sim 0°$ in the southern hemisphere and $\alpha \sim 180°$ in the northern hemisphere), (e) are accompanied by the low-energy H^+ flux enhancements that have lower energies than O^+ by a factor of 3–10, and (f) increase the O^+ density and the O^+/H^+ density ratio by ~10 times and 4–5 times, respectively. We perform a numerical simulation to trace ion trajectories forward in time from the Arase positions. It is revealed that both H^+ and O^+ ions drift eastward and reach the dawn-to-morning sector without being lost in the ionosphere, if the pitch angle scattering effect is considered near the equatorial plane. This result suggests that these low-energy field-aligned ions can contribute to formation of the warm plasma cloak.

1. Introduction

Recent studies employing the Van Allen Probes have shown that unidirectional/bidirectional energy-dispersed O^+ flux appears in the inner magnetosphere during disturbed periods with a decrease in its energy from ~5 keV to 10 eV (Chaston et al., 2015; Gkioulidou et al., 2019; Hull et al., 2019; Kistler et al., 2016; Nosé et al., 2016). Chaston et al. (2015) reported energized outflowing/bouncing ionospheric ions in the inner magnetosphere ($L \sim 3.0$–6.5) during the main phase of a geomagnetic storm on June 1, 2013 ($Dst_{min} = -124$ nT). The field-aligned ion flux enhancements streaming outward from the ionosphere were observed at energies below 1 keV for H^+ and at larger energies (possibly < 5 keV) for O^+ with the energy-dispersed signature. Kistler et al. (2016) examined the same event and discussed that the dispersion is most likely temporal and due to a burst of outflow over a broad energy range, with the fastest ions reaching the Van Allen Probes first. Gkioulidou et al. (2019) found bidirectional field-aligned H^+ and O^+ flux enhancements near perigee (inside $L \sim 4$) during the main phase of a geomagnetic storm on June 23, 2015 ($SYM\text{-}H_{min} = -208$ nT). These enhancements exhibited energy dispersion and multiple bands at low energy (<keV). It was concluded that they are due to O^+ ions exiting from both hemispheric ionospheres within $L \sim 3$–4, directly entering the inner magnetosphere, and subsequently bouncing between hemispheres. Hull et al. (2019) showed antiparallel O^+ flux spectra at energies ranging from tens of keV down to 10 eV dung a storm of June 28–30, 2013 ($SYM\text{-}H_{min} = -111$ nT), which are due to outflowing O^+ ions from the northern ionosphere. In these previous studies, only a single event during storm time has been examined. However, Nosé et al. (2016) statistically studied 74 events of dipolarization and found that the unidirectional energy-dispersed O^+ flux at 0.1–5 keV was observed in 80% of the total events. The direction of flux is parallel (antiparallel) to the magnetic field when the Van Allen Probes are located below (above) the geomagnetic equator. This strongly implies that these O^+ ions are extracted from the ionosphere at the onset of substorms and flow along the magnetic field toward the geomagnetic equator.

As shown above, the Van Allen Probes observations revealed that O^+ fluxes are enhanced in the field-aligned direction in the energy range from ~10 eV to a few keV at substorm onset. However, it is not yet clear where these field-aligned low-energy ions travel. If they become the constituent of the inner magnetospheric plasma, the ion composition there may be altered because they are dominant in O^+ ions. In this case, various phenomena occurring in the inner magnetosphere such as electromagnetic ion cyclotron waves, standing Alfvén waves along the geomagnetic field, and magnetospheric/plasmaspheric cavity resonance, will change their characteristics or excitation condition. Therefore, further studying the field-aligned low-energy O^+ ions in terms of their transport path and fate is important for exact understanding of inner magnetospheric physics.

The similar O^+ flux enhancement was also observed by the Exploration of energization and Radiation in Geospace (ERG) "Arase" satellite at a radial distance (r) of 4.3–4.6 R_E, geomagnetic latitude (GMLAT) of 16°–18°, and magnetic local time (MLT) of 5.5–5.7 h around 15:00 UT on March 27, 2017 (Nosé, Matsuoka, Kasahara, et al., 2018). In this event, magnetic field dipolarization was followed by the O^+ flux enhancements in the direction near parallel or antiparallel to the magnetic field line at ≤15 keV. This is a case study based on observation made in the very beginning phase of the Arase mission after its launch on December 20, 2016. Instead, in the present study, we intend to statistically examine the low-energy O^+ flux enhancements, using the magnetic field and ion flux data obtained by the Arase satellite. Numerical calculation of ion trajectories is also performed to find the destination of the low-energy O^+ ions.

The rest of the paper is organized as follows. In Section 2, we describe the data set used in this study and introduce the event selection procedure. From a 14-month period, we identified 55 events of the low-energy O^+ flux enhancements that have energy-dispersed signatures with decreasing energy from a few keV to 10–100 eV and appear after magnetic field dipolarization. Section 3 details three typical events of the low-energy ion flux enhancements. In Section 4, we perform statistical analyses for the 55 events to examine geomagnetic condition, pitch angle distribution, and change of ion composition of these flux enhancements. Section 5 gives results of numerical simulation, in which trajectories of ions are traced forward in time from the Arase position to identify their destination. In Section 6, we compare the Arase observations with those reported by previous studies. On the basis of the results from both the observations and the numerical simulation, we also discuss a possible link between the field-aligned low-energy O^+ flux enhancements and the warm plasma cloak or the oxygen torus. Section 7 summarizes the present study.

2. Data Set and Event Selection

2.1. Magnetic Field Data and Low-Energy Ion Flux Data From Arase Satellite

The Arase satellite has an elliptical orbit with a perigee of ~400-km altitude, an apogee of 6.0 R_E, an inclination of 31°, and an orbital period of 9.5 h (Miyoshi, Shinohara, et al., 2018). It was launched on December 20, 2016 and has been in operation for ~4 years since the end of March 2017 (as of January 2021). In this study, we used the Arase data for the periods of April 1–October 31, 2017 and July 1, 2018–January 31, 2019 (429 days in total). Figure 1 shows the Arase orbits on the first and sixteenth days of each month and the final days during these periods in the x-y and x-z planes in solar magnetic (SM) coordinates (Miyoshi, Shinohara, & Jun, 2018). The orbital apogee covers the MLT range from the predusk to predawn centered around 23 MLT, where the magnetic field dipolarization is frequently observed (Kokubun & McPherron, 1981; Nagai, 1982). In the period of April 1–October 31, 2017, Arase mostly stayed in the northern hemisphere (GMLAT ≥ 0°), while in the period of July 1, 2018–January 31, 2019, its apogee was located for a longer time in the southern hemisphere (GMLAT < 0°). We do not use data from the period of November 1, 2017–June 30, 2018, because during this period Arase had the apogee on the dayside and dawnside, where only a few events of dipolarization are expected to occur.

Arase carries the fluxgate magnetometer (MGF) (Matsuoka, Teramoto, Nomura, et al., 2018) to measure the magnetic field. This study uses the Arase/MGF data with a cadence of the satellite spin period (~8 s) in VDH coordinates, where H is antiparallel to the dipole axis, V points radially outward and is parallel to the magnetic equator, and D is eastward and completes a right-handed orthogonal system (Matsuoka, Teramoto, Imajo, et al., 2018). The magnitude of the measured magnetic field in the inner magnetosphere sometimes shows rapid changes, which are largely due to the motion of satellites. These rapid changes can

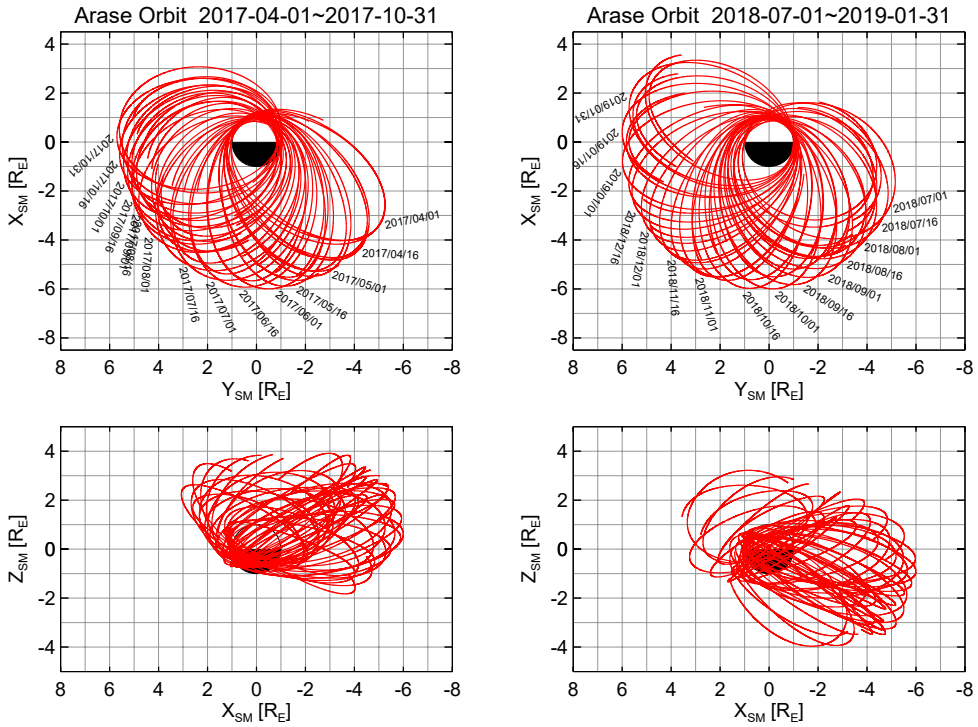

Figure 1. Orbit of the Arase satellite on the first and sixteenth days of each month and the final day during April 1–October 31, 2017 (left) and July 1, 2018–January 31, 2019 (right) in the x-y and x-z planes in solar magnetospheric coordinates.

be much larger than variations of dipolarization and mask them. To remove this spatial effect from the measured magnetic field, it is better to use a static magnetic field model. Therefore, for the sake of easy identification of dipolarization events, we calculate the magnetic field deviation (ΔV, ΔD, and ΔH) from the International Geomagnetic Reference Field (IGRF)-13 internal model field (Alken et al., 2021) and the Tsyganenko T89 external model field (Tsyganenko, 1989) with Kp = 0 (Matzka et al., 2021).

Arase also carries the low-energy particle experiments–ion mass analyzer (LEPi) (Asamura, Kazama, et al., 2018), which is composed of an electrostatic energy-per-charge (E/q) analyzer and a time-of-flight (TOF) section to measure ion fluxes in the energy range of 0.01–25 keV/q with discrimination of ion species. The LEPi has a planar field-of-view and provides 4π sr coverage by using the spin motion of the satellite. It has 15 azimuthal channels with a width of angular response of 4.3° (narrow channel) or 16.0° (wide channel) arranged at an angular separation of 22.5°. The one spin period is divided into 16 spin phases, in each of which the E/q range is swept with 32 logarithmically spaced energy steps to obtain the energy spectra of ions. LEPi has two observation modes: normal mode and TOF mode. This study uses the Arase/LEPi data in the normal mode, in which the three-dimensional velocity distribution functions of ions can be obtained once per spin (Asamura, Miyoshi, & Shinohara, 2018).

2.2. Magnetic Field Dipolarization

It has been reported that the low-energy O^+ flux enhancement appears a few minutes after dipolarization in the inner magnetosphere (Nosé et al., 2016, Nosé, Matsuoka, Kasahara, et al., 2018). Thus, we first select the magnetic field dipolarization events with the following three criteria: (a) Arase is located at 18:00–04:00 MLT and $L \geq 4.0$, (b) ΔH is increased by more than 20 nT in 10 min, and (c) substorm signatures are identified in the geomagnetic AE or Wp index (Nosé et al., 2012; World Data Center for Geomagnetism, Kyoto, et al., 2015, 2016), which reflects the high-latitude negative bays or the low-latitude Pi2 pulsations. These criteria identified 192 events of the magnetic field dipolarization in the inner magnetosphere.

Figure 2a shows the dwell time of Arase during the 429 days in MLT-L plane. We find that Arase stayed more than 1 day in almost all MLT-L meshes and made observations for ≥6.8 days in all MLT bins near its apogee (L = 5.5–6.5). Figure 2b is the dwell time of Arase in L-GMLAT plane. Because of its high orbital inclination, Arase does not cover the near-equatorial region at L = 6.5–8.0. Instead, there are L-GMLAT meshes with longer dwell time extending from (L, |GMLAT|) = (5.5–6.0, 0°–10°) to (7.0–8.0, 20°–30°). Figure 2c gives Arase location for the selected 192 events of the magnetic field dipolarization in the L-MLT plane. The events are found over wide ranges of both L and MLT with the dominance at $L \geq 6.0$ and premidnight. From the results of Figures 2a–2c, we calculate the occurrence probability of the magnetic field dipolarization as a function of MLT (Figure 2d) and L (Figure 2e). It is found that the occurrence probability of dipolarization has a peak at MLT = 22–23 h and decreases as the satellite moves away toward dusk or predawn. The L dependence of the occurrence probability shows a generally monotonic increase from L = 4.0–4.5 to larger L and had a peak at L = 7.5–8.0. Here it should be noted that Arase made observations only in the off-equatorial regions (|GMLAT| ≥ 15°) at L = 6.5–8.0 (Figure 2b), where the dipolarization events are more difficult to identify with criteria (b). Thus, it is likely that the occurrence probability at L = 6.5–8.0 shown in Figure 2e is underestimated and that the L dependence has a steeper positive gradient. These characteristics of the occurrence probability are consistent with those reported by previous studies (e.g., Kokubun & McPherron, 1981; Lopez et al., 1988; Nagai, 1982; Nosé et al., 2010), indicating that the dipolarization events are properly selected with the above criteria.

2.3. Low-Energy O^+ Flux Enhancement Accompanied With Dipolarization

Out of the selected 192 events of dipolarization, we find that LEPi obtains the three-dimensional velocity distribution of H^+ and O^+ (i.e., the normal mode) for 153 events. These events are visually examined if they are accompanied with low-energy O^+ flux enhancements that have energy-dispersed signatures with decreasing energy from a few keV to 10–100 eV. Finally, we select 55 such events. Typical examples of these events are introduced in the next section.

3. Event Study of Low-Energy O^+ Flux Enhancements

3.1. July 22, 2017 Event at L = 6.6–5.7 Above Equatorial Plane (Event 1)

Figure 3 displays one of the selected 55 events of the low-energy O^+ flux enhancements, which is found during 17:00–18:00 UT on July 22, 2017 when Arase is located at MLT = 22.8–23.9 h and L = 6.6–5.7 above the equatorial plane (GMLAT = 22.1°–22.8°). From top to bottom, displayed are the SYM-H index (Figure 3a), the Wp index (Figure 3b), the magnetic field deviation from the model field in VDH coordinates (ΔV, ΔD, and ΔH) (Figure 3c), the energy-time (E-t) spectrograms of H^+ at different pitch angles (α) of 0°–30°, 75°–105°, and 150°–180° (Figures 3d–3f), the pitch angle-time (α-t) spectrogram of H^+ at energy of 13–32 eV (Figure 3g), the E-t spectrograms of O^+ at α = 0°–30°, 75°–105°, and 150°–180° (Figures 3h–3j), the α-t spectrogram of O^+ at energy of 56–131 eV (Figure 3k), and the H^+ and O^+ densities as well as the O^+/H^+ density ratio (Figure 3l). Here it should be noted that the densities are computed from ion flux data over the energy range of 0.01–3 keV and may be referred to as partial densities in the strict sense. This energy range is chosen to examine density variations that are associated with the low-energy flux enhancements. In this 2-hour interval, the OMNI data (not shown here) indicate that the solar wind conditions were rather stable with northward IMF ($B_z \sim$ 0–5 nT) and small dynamic pressure ($P_{dy} \sim$ 2–3 nPa).

Figure 3a shows that this event occurred during a non-storm period (SYM-H = −7 to −17 nT), as expected from the solar wind conditions. Dotted magenta lines indicate that ΔH shows clear increases at 17:06 UT, 17:23 UT, and 17:40 UT (Figure 3c), each of which is preceded by an enhancement of the Wp index (Figure 3b), that is, low-latitude Pi2 pulsations. Therefore, we think that three dipolarization events intermittently occurred during 17:00–18:00 UT, although the first two events do not satisfy the criterion of ΔH (≥20 nT in 10 min) and are not included in the selected 55 events.

From the E-t spectrograms of O^+ ions (Figures 3h–3j), we note that O^+ flux shows distinct energy-dispersed flux enhancements in the direction antiparallel to the magnetic field (α = 150°–180°). These O^+

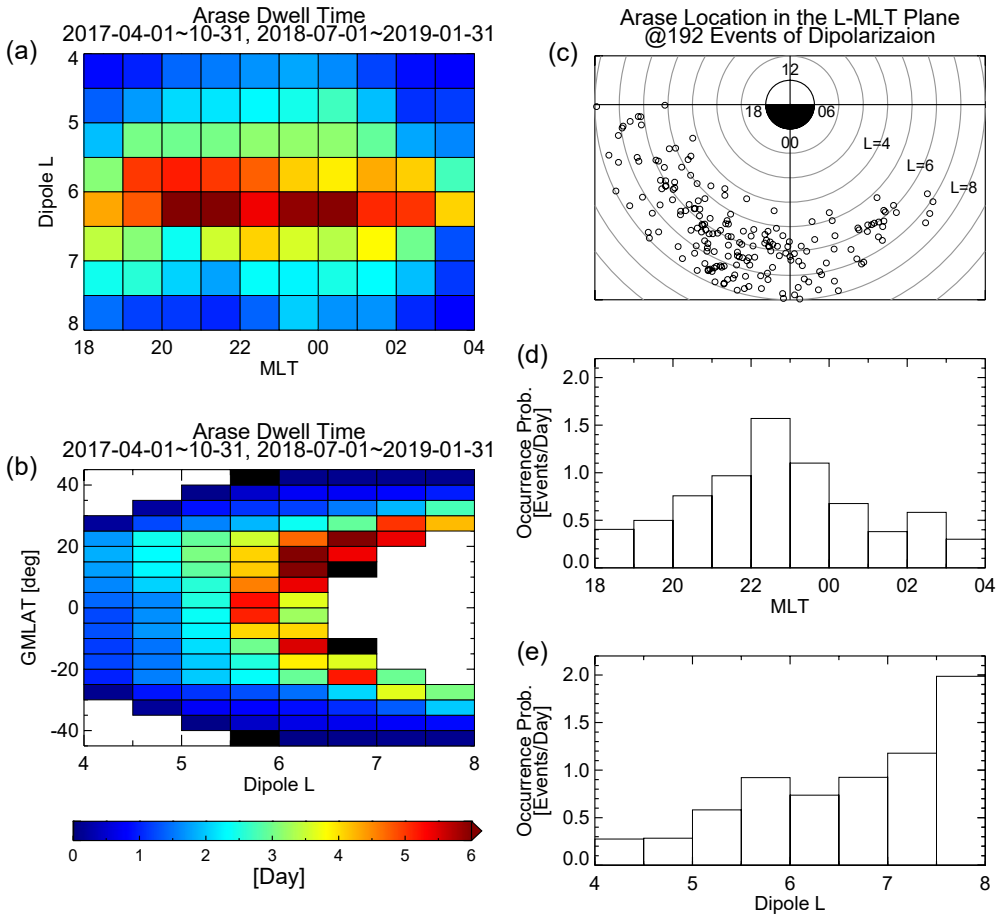

Figure 2. (a) Dwell time of Arase during April 1–October 31, 2017 and July 1, 2018–January 31, 201 in magnetic local time (MLT)-*L* plane. (b) Dwell time of Arase in *L*-geomagnetic latitude plane. (c) Location of Arase in the *L*-MLT plane when the 192 events of the magnetic dipolarization are identified. (d) MLT dependence of the occurrence probability of the dipolarization. (e) *L* dependence of the occurrence probability of the dipolarization. The occurrence probability is calculated from the number of events divided by the dwell time of Arase in each bin.

flux enhancements start 2–3 min after the second and third events of dipolarization (around 17:25 UT and 17:43 UT) and continues until 17:40 UT and 18:20 UT. The energy decreased gradually from a few keV to ~200 eV (for the second event) or ~20 eV (for the third event). For the first event, we notice a subtle O^+ flux increase in the energy of 3 keV–300 eV between 17:10 UT and 17:21 UT (Figure 3j), which may be also related to the energy-dispersed flux enhancement. From the α-*t* spectrogram of Figure 3k, we find that these antiparallel fluxes are nearly collimated along the magnetic field direction ($\alpha \sim 180°$) at 56–131 eV. In Figure 3h, there are other energy-dispersed flux enhancements at energies between a few keV and 200 eV at $\alpha = 0°$–$30°$, but they are low in flux and appear later in time. Thus, we suppose that the energy-dispersed O^+ flux enhancements are dominant in the antiparallel direction ($\alpha \sim 180°$) and the energies from a few keV to ~20 eV.

From the *E*-*t* and α-*t* spectrograms of H^+ ions (Figures 3d–3g), we find that flux enhancements occur predominantly in the antiparallel direction ($\alpha \sim 180°$) and lower energies (1 keV–10 eV) with the energy-dispersed signature, which are similar to characteristics of O^+, although their dispersion is steeper than that of O^+.

In Figure 3l, for the second event, the O^+ density (red line) is significantly enhanced after 17:23 UT in association with the low-energy O^+ flux enhancement, while the H^+ density (black line) shows a moderate increase. This results in an enhancement of the O^+/H^+ density ratio (blue line) to ~0.10. For the third event,

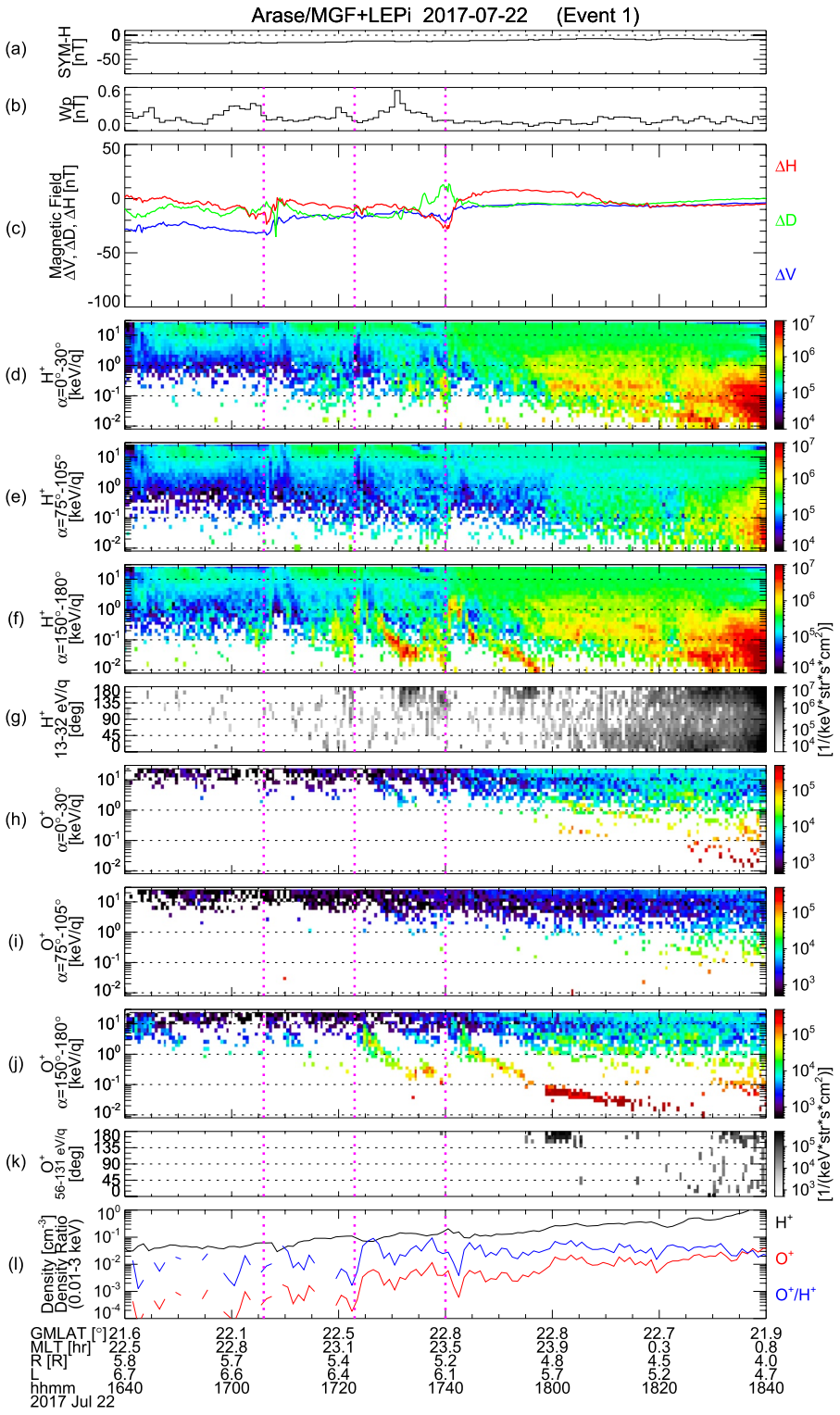

Figure 3. Geomagnetic indices and the Arase data during 16:40–18:40 UT on July 22, 2017 (event 1). From top to bottom displayed are (a) the SYM-H index, (b) the Wp index, (c) the magnetic field deviation from the model field in VDH coordinates (ΔV, ΔD, and ΔH), (d–f) the energy-time spectrograms of H^+ at different pitch angles of 0°–30°, 75°–105°, and 150°–180°, (g) the pitch angle-time spectrogram of H^+ at energy of 13–32 eV (h–j) the energy-time spectrograms of O^+ at different pitch angles of 0°–30°, 75°–105°, and 150°–180°, (k) the pitch angle-time spectrogram of O^+ at energy of 56–131 eV, and (l) the H^+ and O^+ densities as well as the O^+/H^+ density ratio. The densities are computed from ion flux data over the energy range of 0.01–3 keV. The magnetic field dipolarization are observed at 17:06 UT, 17:23 UT, and 17:40 UT as indicated with dotted magenta lines, when Arase is located at L = 6.6–5.7 above the equatorial plane.

immediately after the dipolarization at 17:40 UT, the energy-dispersed O^+ flux enhancement related to the second event disappears as seen in Figure 3j and the O^+ density shows a sharp drop to approximately 10^{-3} cm^{-3}, which is considered to be the O^+ density of the background plasma. After 17:43 UT, the energy-dispersed O^+ flux enhancement starts to appear and contributes to the O^+ density enhancement. In particular, the O^+ density shows a clear increase around 18:00 UT, which is caused by the large O^+ flux at <100 eV. The H^+ density increase is gradual and less significant than that of O^+, leading to an enhancement of the O^+/H^+ density ratio to 0.05–0.08. In summary, because of the energy-dispersed O^+ flux enhancements, the O^+/H^+ density ratio can reach 0.05–0.10 around $L = 5.0$–6.3.

We note from Figures 3f and 3j that the flux enhancements seem to occur at higher energy for O^+ than H^+. To examine the energy difference in more detail, we compare the energy spectra between H^+ and O^+. Figures 4a and 4b display the spectra of H^+ (black line) and O^+ (red line) at $\alpha = 150°$–180° during ~5 min intervals starting around 17:30 UT and 17:50 UT, respectively. Around 17:30 UT, H^+ flux has a peak at 48.5 eV, while O^+ flux has a peak at 201.4 eV, resulting in a larger peak energy of O^+ by a factor of ~4.2. Around 17:50 UT, peak energies are 35.8 eV for H^+ and 201.4–356.0 eV for O^+, again giving a larger peak energy of O^+ by a factor of 5.6–9.9.

3.2. July 16, 2017 Event at $L = 6.0$ Above Equatorial Plane (Event 2)

Figure 5 shows another example of the low-energy O^+ flux enhancements observed above the equatorial plane. The format is the same as in Figure 3 except for the time interval of 15:40–17:40 UT on July 16, 2017. In Figure 5b, the AL index replaces the Wp index, because a substorm signature is identified clearly as a high-latitude negative bay in this event. According to the OMNI data (not shown here), IMF B_z had a rather constant value of about −10 nT before 15:40 UT, increased to ~0 nT at 15:50 UT, and then showed fluctuations between −5 nT and 5 nT afterward. The solar wind dynamic pressure was steady at ~1.5 nPa.

The SYM-H index (Figure 5a) is increasing approximately −70 nT to −40 nT, indicating a recovery phase of a magnetic storm, which is consistent with the IMF B_z signature. A decrease of the AL index (Figure 5b) and the magnetic field dipolarization in the inner magnetosphere (Figure 5c) are observed simultaneously at 1605 UT, when Arase is located at MLT = 21.0 h, $L = 6.0$, and GMLAT = 14.5°. In the *E-t* spectrograms of H^+ and O^+ fluxes at three different α (Figures 5d–5f and 5h-5j), low-energy ion flux enhancements appear only in the antiparallel direction from 16:20 UT for about 1 h with the energy-dispersed signatures. The O^+ energy decreases from 1 keV to ~30 eV, while the H^+ energy decreases from 200 to ~20 eV. The pitch angle distribution displayed in Figures 5g and 5k indicates that these flux enhancements are dominated by ions with $\alpha \sim 180°$.

In Figure 5l we find the large values of the O^+ density and the O^+/H^+ density ratio at 15:40–16:00 UT. They are due to the O^+ flux enhancement that occurred before event 2, as can be seen in Figure 5j. This O^+ flux enhancement disappears at 16:00–16:05 UT and the O^+ density returns to the background level of ~10^{-3} cm^{-3} at 16:05 UT. This signature is very similar to that seen at 17:40–17:42 UT of event 1 (Figure 3l). After 16:05 UT, the O^+ density is more clearly increased than the H^+ density during the low-energy flux enhancements, leading to the enhancement of the O^+/H^+ density ratio from ~0.02 at 16:05 UT to ~0.1 at 16:25–17:20 UT ($L = 6.3$–6.8).

The energy difference between the H^+ and O^+ flux enhancements at $\alpha = 150°$–180° is examined for ~5 min intervals starting around 16:30 UT (Figures 4c) and 16:50 UT (Figure 4d). Peak energies around 16:30 UT are 64.5 eV for H^+ and 473.2 eV for O^+, and the energy is ~7.3 times larger for O^+. Peak energies around 16:50 UT are 35.8–64.5 eV for H^+ and 201.4 eV for O^+, and the O^+ energy is 3.1–5.6 times larger than the H^+ energy.

3.3. November 4, 2018 Event at $L = 5.1$ Below Equatorial Plane (Event 3)

Figure 6 shows the low-energy O^+ flux enhancements observed below the equatorial plane for the time interval of 20:20–22:20 UT on November 4, 2018, in the same format as in Figure 3. The OMNI data indicate

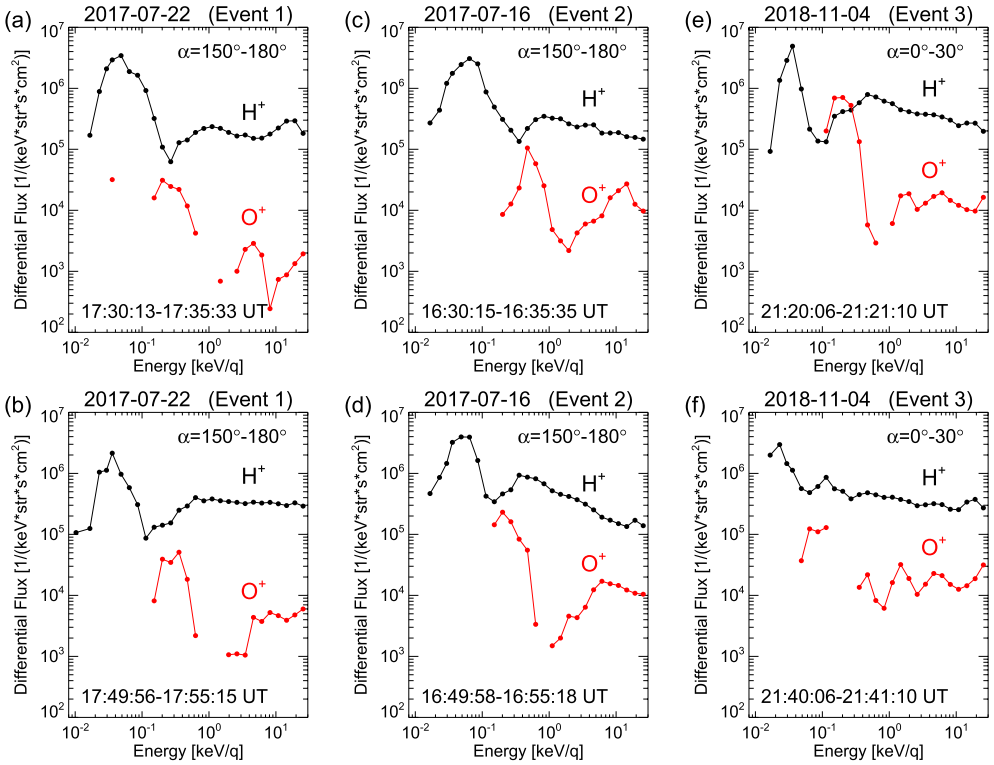

Figure 4. Energy spectra for H^+ (black line) and O^+ (red line) at pitch angle of 150°–180° for (a) 17:30:13–17:35:33 UT and (b) 17:49:56–17:55:15 UT on July 22, 2017 (event 1), and for (c) 16:30:15–16:35:35 UT and (d) 16:49:58–16:55:18 UT on July 16, 2017 (event 2). Energy spectra for H^+ and O^+ at pitch angle of 0°–30° for (e) 21:20:06–21:21:10 UT and (f) 21:40:06–21:41:10 UT on November 4, 2018 (event 3).

gradual increases of both IMF B_z (from approximately −10 to ∼7 nT) and P_{dy} (from ∼5 nPa to ∼8 nPa) for 20:20–21:30 UT, although the data are unavailable after 21:30 UT.

This event occurs between SYM-H = −26 nT and −8 nT (Figure 6a). An overall gradual increase of the SYM-H index is expected from the solar wind condition. The magnetic field dipolarization starts at 2054 UT on November 4, 2018 (Figure 6c), which is accompanied by enhancements of the Wp index (Figure 6b). This event is found at MLT = 20.0 h, L = 5.1, and GMLAT = −17.2°. From the E-t and α-t spectrograms for H^+ and O^+ (Figures 6d–6k), we find energy-dispersed flux enhancements predominantly in the parallel direction. The H^+ and O^+ flux enhancements appear at ∼0.5 and ∼5 keV, respectively, a few minutes after the dipolarization. Their energies are gradually decreased to ∼20 eV in 1 h. There is an antiparallel flux enhancement in Figure 6f but it appears more than 40 min after the dipolarization.

Figure 6l shows the large values of the H^+ and O^+ densities before 20:50 UT. They are caused by strong flux enhancements at <100 eV as seen in Figures 6d–6f and 6h–6j. According to a plasma wave spectrogram from the Plasma Wave Experiment (Kumamoto et al., 2018) on board Arase (not shown here), the satellite was within the plasmasphere before 20:22 UT and traversed the plasmapause between 20:22 UT and ∼20:50 UT. Thus, the strong flux enhancements are interpreted as thermal plasma in the outer plasmasphere reported by Comfort (1996) and Craven et al. (1991). After 20:50 UT, they vanish and the O^+ density becomes to the background level of $\sim 2 \times 10^{-3}$ cm^{-3} at 20:54–20:55 UT. After the dipolarization, there is a clear increase of the O^+ density with an almost constant H^+ density, resulting in an increase of the O^+/H^+ density ratio from ∼0.01 at ∼20:54 UT to ∼0.2 at 21:00–22:20 UT (L = 5.2–5.9).

The energy spectra of H^+ and O^+ at α = 0°–30° are displayed for ∼1 min intervals around 21:20 UT (Figures 4e) and 21:40 UT (Figure 4f). In corresponding time intervals, we find peak energies of H^+ at 35.8 and 23.0 eV, and peak energies of O^+ at 151.5–201.4 eV and 64.5–114.0 eV. Thus, the energy difference between O^+ and H^+ is a factor of 4.2–7.5 and 2.8–5.0.

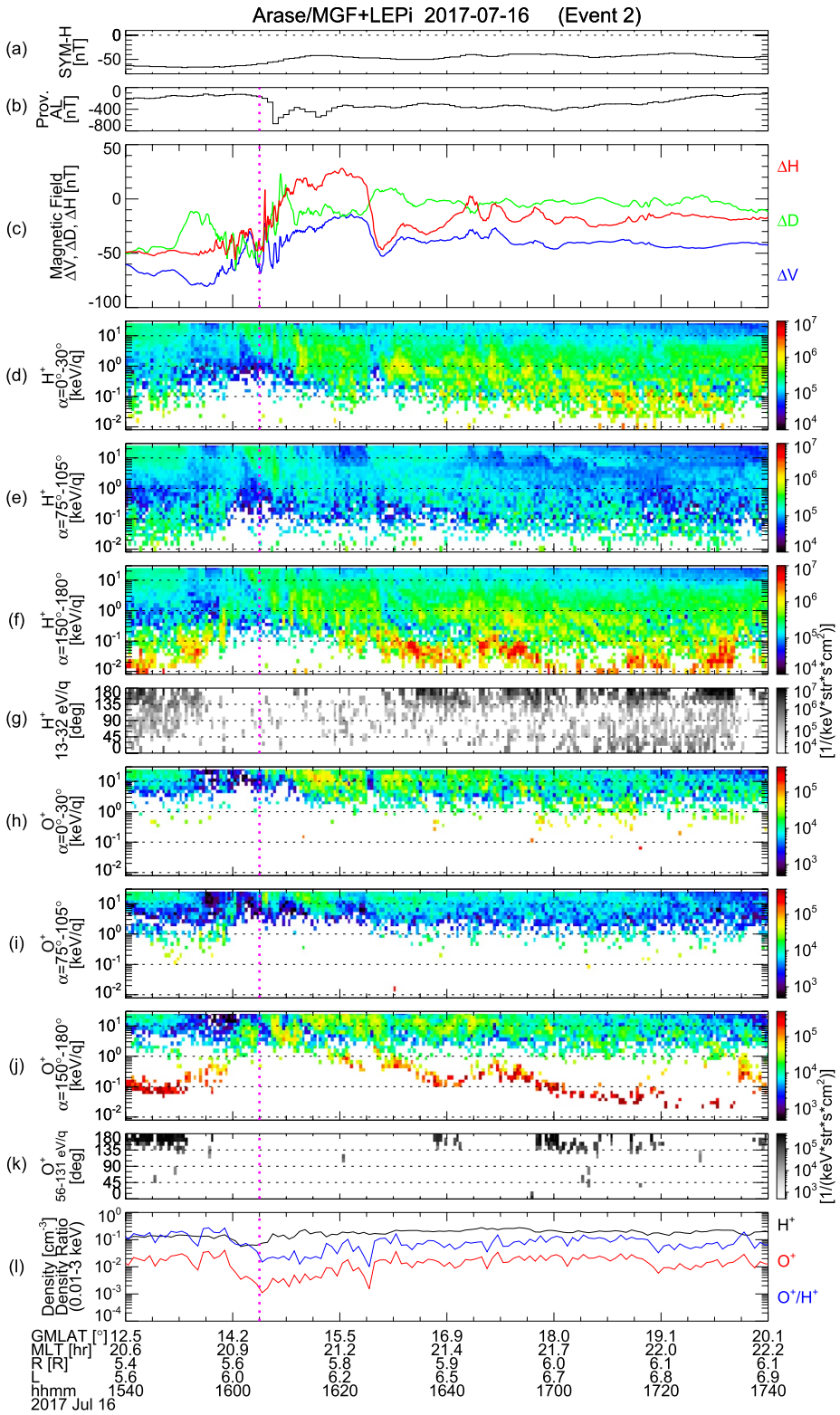

Figure 5. Same as Figure 3 but for the time interval of 15:40–17:40 UT on July 16, 2017 (event 2). The provisional AE index is plotted instead of the Wp index. The magnetic field dipolarization is observed at 16:05 UT (dotted magenta line), when Arase is located at $L = 6.0$ above the equatorial plane.

4. Statistical Study of Low-Energy O^+ Flux Enhancements

4.1. Geomagnetic Condition

Chaston et al. (2015), Gkioulidou et al. (2019), Hull et al. (2019), and Kistler et al. (2016) reported the low-energy O^+ flux enhancement events during large magnetic storms (SYM-H of −100 nT to −200 nT), although events 1 and 3 are identified during the SYM-H index was larger than −30 nT (Figures 3a and 6a). We statistically examine geomagnetic conditions for the 55 events to check if geomagnetic storm is necessary for the occurrence of the low-energy O^+ flux enhancements in the inner magnetosphere.

Figure 7a shows a result of the superposed epoch analysis of the SYM-H index for the 55 events during the period of $T = -30$–60 min, where the zero epoch time ($T = 0$ min) represents the onset of the dipolarization. We plot values of individual events (gray lines), the average (thick line), and the standard errors (thin lines). The average value of the SYM-H index is approximately −30 nT. More than half of events (30 events) have SYM-H > −30 nT for the 90 min interval. There are only seven events in which the SYM-H index stays below −50 nT. In Figure 7b, the SYM-H index is shown for these seven events between $T = -360$ and 720 min. Different colors are used for a visual aid. Only one event delineated with a red curve is identified during the storm main phase. In other six events, SYM-H gradually increases, indicating that they occur during the recovery of magnetic storms. These results confirm that the low-energy O^+ flux enhancement frequently occur during non-storm periods and the storm recovery phase. We think that the magnetic storm condition is not essential to the low-energy O^+ flux enhancements.

4.2. Direction of Flux Enhancement

In the previous section, we find the O^+ flux enhancements in the antiparallel direction for events 1 and 2, and in the parallel direction for event 3. According to the direction of flux enhancements, the 55 events are classified into two categories: the antiparallel flow and the parallel flow. When the flux enhancements appear in both the antiparallel and parallel directions (e.g., event 1, Figures 4h and 4j), a direction with a larger and earlier flux enhancement is adopted as the flow direction. In the 55 events, there are no "mixed flow" events that are composed of flux enhancements in two or three pitch angle ranges with similar magnitude and at the same time, although Nosé et al. (2016) found three such events near the equatorial plane from the Van Allen Probes observations. Figure 8 shows the location of 55 events in the meridional plane with colors to denote the flow direction (green for the antiparallel direction and orange for the parallel direction). The antiparallel flow events are observed above the geomagnetic equator, while the parallel flow events are observed below the geomagnetic equator except for two events. This statistical result strongly implies that low-energy O^+ ions are extracted from the ionosphere at the onset of substorms and flow along the magnetic field toward the geomagnetic equator.

It is noteworthy to briefly mention the north-south asymmetry in the number of the events seen in Figure 8. There are 45 events in the northern hemisphere and 10 events in the southern hemisphere. We suppose this asymmetry is caused by two factors: Arase dwell time and geomagnetic activity. In Figure 2b, we find the north-south asymmetry of the Arase dwell time with 117.2 days at GMLAT ≥ 0° and 85.6 days at GMLAT < 0°. Geomagnetic activity measured by the average value of the Kp index is 1.86 for the period of April 1–October 31, 2017 when Arase was mostly flying at GMLAT ≥ 0°, and 1.40 for the period of July 1, 2018–January 31, 2019 when the Arase orbit was skewed toward GMLAT < 0° (Figure 1). Thus, the longer dwell time of Arase and more disturbed geomagnetic condition in the northern hemisphere (GMLAT ≥ 0°) results in the observed north-south asymmetry in the number of events.

4.3. Ion Composition Change

The change of the density and the density ratio is statistically examined in the course of the O^+ flux enhancements. Figures 9a–9c respectively show results of the superposed epoch analysis of the H^+ density, the O^+ density, and the O^+/H^+ density ratio. Since these values are expected to depend on the Arase location or geomagnetic conditions, they are normalized by the values before the dipolarization, that is, the average at $T = -5$ to 0 min. We remove time intervals when the H^+ density became less than 0.1 cm^{-3}, because Arase is considered to be located near the magnetic lobe in such intervals. In each panel of Figure 9, plotted are

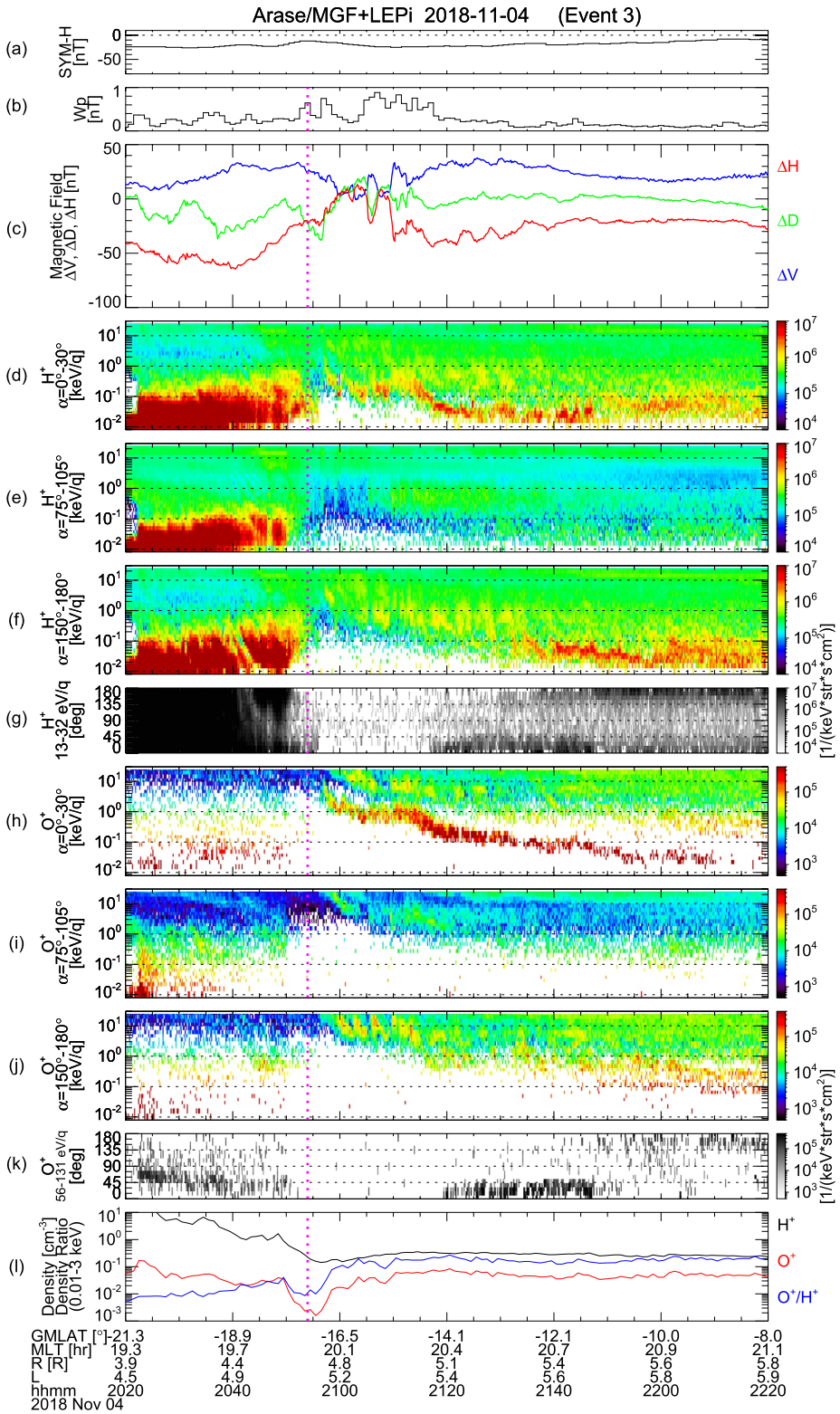

Figure 6. Same as Figure 3 but for the time interval of 20:20–22:20 UT on November 4, 2018 (event 3). The magnetic field dipolarization is observed at 20:54 UT (dotted magenta line), when Arase is located at $L = 5.1$ below the equatorial plane.

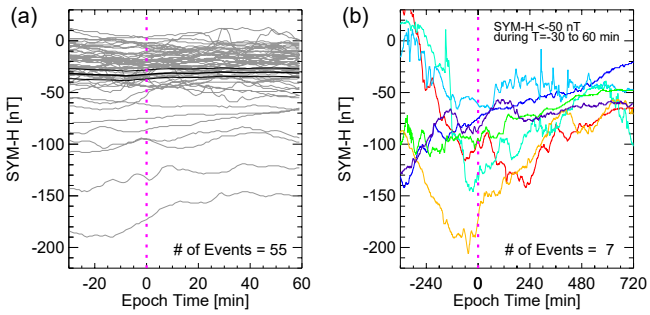

Figure 7. (a) Results of the superposed epoch analysis of the SYM-H index for the 55 events during the period of $T = -30$–60 min, where the zero epoch time ($T = 0$ min) marks the onset of the dipolarization. Data of individual events are displayed with gray lines. Averages and standard errors are shown with thick and thin lines, respectively. (b) The SYM-H index for the seven events, in which SYM-H < −50 nT in Figure 7a, during the period of $T = -360$–720 min. Different colors are used for a visual aid.

the density or density ratio of individual events (dotted gray lines), its averages (thick line), and its standard errors (thin lines). The H^+ density increases ~3 times within $T \sim 30$ min. The O^+ density also increases over the same time interval but more prominently, reaching ~10 times. Correspondingly, in Figure 9c, the O^+/H^+ density ratio is enhanced by a factor of 4–5 for $T = 30$–60 min. These results indicate that the low-energy ion flux enhancement associated with dipolarization contains more O^+ ions than the background plasma in the inner magnetosphere.

One may note from Figure 9b that a few events have overall smaller values of the O^+ density than the preonset level (<0.5) after $T = 20$ min. We find that these events exhibit a short duration of the energy-dispersed O^+ flux enhancements (<30 min) and occur during the Arase outbound orbits. Such short duration of the O^+ flux enhancement does not contribute to the density increase at $T \sim 30$–60 min. The outbound motion of Arase is likely to cause the gradual decrease of the O^+ density, because the O^+ density becomes smaller in the outer magnetosphere (e.g., Lennartsson, 1989). Thus, we suppose that these are possible reasons for the smaller values of the O^+ density. However, these events are just minor and make little impact on the results of the superimposed epoch analysis shown in Figures 9b and 9c.

5. Numerical Simulation for Trajectories of Field-Aligned Low-Energy Ions

Arase identifies the field-aligned low-energy H^+ and O^+ flux enhancements with the energy-dispersed signature after magnetic field dipolarization. We calculate forward trajectories of the field-aligned low-energy ions to find where they travel, using the numerical simulation code developed by Delcourt et al. (1990). The

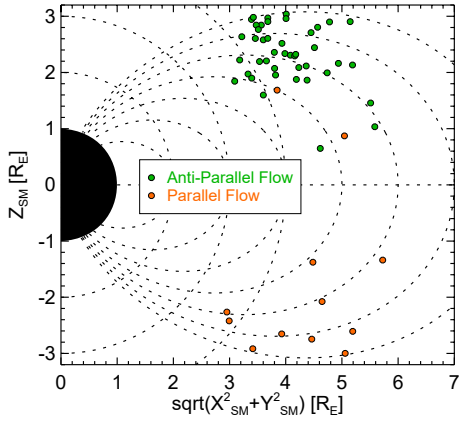

Figure 8. Distribution of the field-aligned low-energy O^+ flux and its flow direction in the geomagnetic meridional plane. Green and orange circles represent a flow in the antiparallel direction and in the parallel direction, respectively.

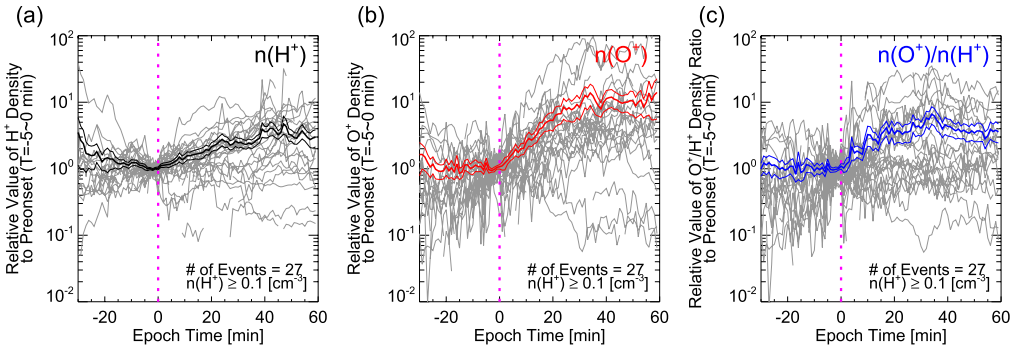

Figure 9. Results of the superposed epoch analysis of (a) the H^+ density, (b) the O^+ density, and (c) the O^+/H^+ density ratio. The zero epoch time denotes the onset of the dipolarization. The densities and the density ratio are normalized by those before the dipolarization, that is, the average over the epoch time of −5 to 0 min. Time intervals when the H^+ density became less than 0.1 cm^{-3} are removed from the analysis. Data of individual events, averages, and standard errors are plotted with dotted gray lines, a thick line, and thin lines, respectively.

simulation code adopts the Tsyganenko T89 external model (Tsyganenko, 1989) field and the Volland-Stern convection electric model field (Maynard & Chen, 1975; Stern, 1975; Volland, 1973) with Kp = 2. The calculation is performed by integration of the guiding center equations of motion until the travel time (t_{travel}) of an ion reaches 10 h or its altitude is less than 300 km (i.e., being lost in the ionosphere).

5.1. Effect of Pitch Angle Scattering Near Equatorial Plane

First, for the sake of simplicity, we calculate the trajectories of O^+ ions with three different initial energies, 1.5 keV, 500 eV, and 100 eV, which start from the identical initial position of (MLT, r, GMLAT) = (23 h, 5.0 R_E, 15°) with $\alpha = 175°$. Results are shown in Figures 10a–10c. In each panel, the ion trajectories are projected onto the X_{SM}-Y_{SM} and X_{SM}-Z_{SM} planes. Circles represent positions of the O^+ ion at specific travel times, which are indicated with different colors as shown in the bottom of figure (Initial and final positions are indicated with brown and magenta.) Open or closed circles mean that the O^+ ion is lost in the ionosphere in the end or continues to travel in the magnetosphere for 10 h. We note that O^+ ions bounce between both hemispheres and travel inward by the $E \times B$ drift, and finally hit the ionosphere within t_{travel} = 1.5–1.9 h. This is because the mirror points of ions become lower in altitude during the inward convection, which is expected from the conservation of both the first and second adiabatic invariants of ions. Thus, in these cases, the field-aligned low-energy ions do not contribute to inner magnetospheric plasma.

Next, we introduce an effect of pitch angle scattering near the geomagnetic equatorial plane. This is because previous satellite studies have reported that strong magnetic field fluctuations are induced during the magnetic field dipolarization near the geomagnetic equator and their characteristic frequency is close to the local gyrofrequency of O^+ ions (Lui & Najmi, 1997; Lui et al., 2008; Nosé et al., 2010, 2014, Nosé, Matsuoka, Kasahara, et al., 2018; Ohtani et al., 1995, 1998; World Data Center for Geomagnetism Kyoto and Nosé, 2016). Such fluctuations would be capable of the pitch angle scattering for O^+ ions. Another possible reason is that the magnetic field configuration continues to be stretched (i.e., taillike) even after the dipolarization if the electromagnetic energy is transferred from the solar wind to the magnetosphere (e.g., Ohtani et al., 1999; Pulkkinen et al., 1998). It is likely that the stretched magnetic field has a small curvature radius near the equator and scatters ions in pitch angle when they pass there. In the numerical calculation, pitch angle is altered toward 90° at $|Z_{SM}| \le 0.5\ R_E$ at the rate of $5°/R_E$, resulting in $\Delta\alpha = 5°$ during an equatorial crossing. This scattering process is effective only in the first equatorial crossing. Figures 10d–10f show ion trajectories when the pitch angle scattering is included. The positions of ions at t_{travel} = 0 h, 2 h, 4 h, 6 h, and 8 h are denoted with brown, purple, blue, green, and yellow circles. As shown with closed magenta circles, O^+ ions survive 10 h in the inner magnetosphere. It is found that all O^+ ions continue to bounce between the hemispheres without being lost in the ionosphere and drift eastward because of their low energies. They spend most time in the midnight to dawn sectors and arrive at MLT ~ 9–10 h. These results reveal that even

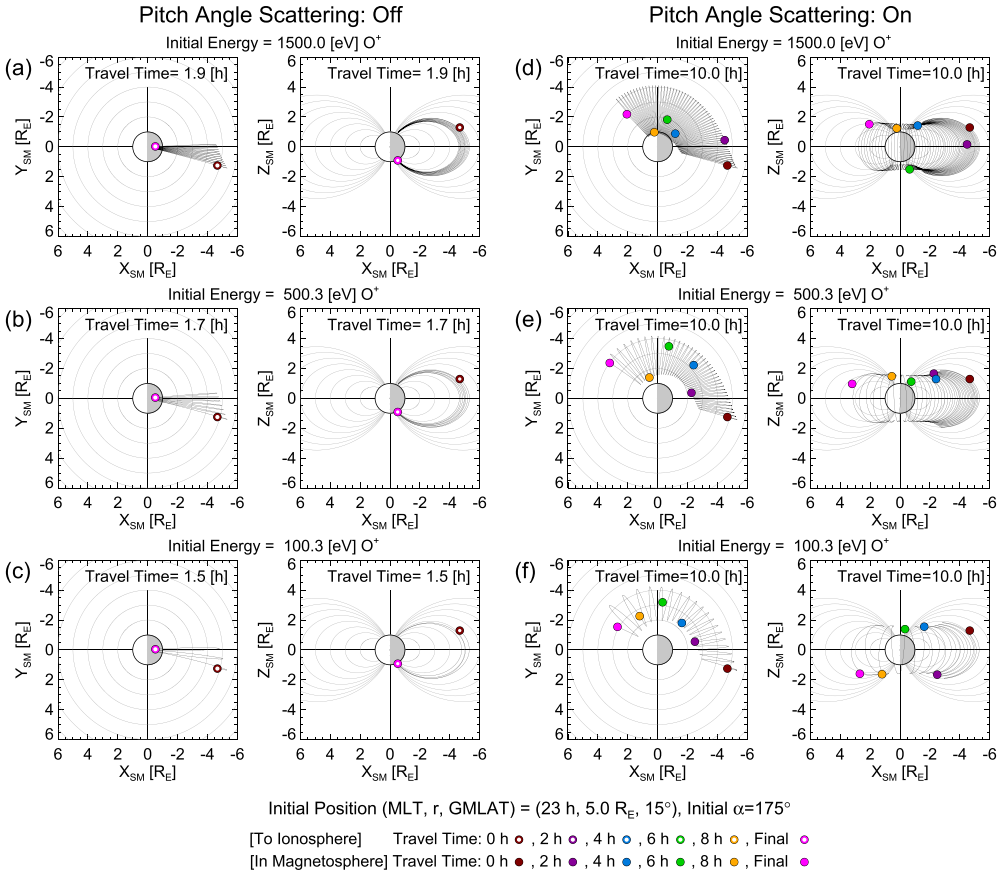

Figure 10. Trajectories of O^+ ions with three different initial energies, (a) 1.5 keV, (b) 500 eV, and (c) 100 eV, which are projected onto (left column) the geomagnetic equatorial plane and (right column) the geomagnetic noon-midnight meridional plane. Pitch angle scattering is not included in the calculation. O^+ ions start from the initial position of magnetic local time = 23 h, $r = 5.0\ R_E$, and geomagnetic latitude = 15° with the pitch angle of 175°. Position of O^+ ion at a specific travel time is indicated with a circle with different colors as shown in the bottom of figure. Open or closed circles mean that the O^+ ion is lost in the ionosphere at last or travels in the magnetosphere for 10 h (d–f) Same as Figures 10a–10c, but the pitch angle scattering is included in the calculation.

small changes of α (i.e., $\Delta\alpha = 5°$) near the equatorial plane can make the field-aligned low-energy O^+ ions contribute to inner magnetospheric plasma in the region extending from midnight to dawn and morning.

5.2. Forward Tracing of Ion Trajectories From Arase Position With Pitch Angle Scattering

We numerically examine where the field-aligned low-energy H^+ and O^+ ions travel after they are observed by Arase. The same pitch angle scattering effect as above is included in the calculation. For event 1, the initial energies of test H^+ and O^+ ions are taken from the peak energies of the field-aligned ion flux enhancement of H^+ (Figure 3f) and O^+ (Figure 3j), respectively, at a given time interval. The test ions start from the Arase positions at the time interval. Similarly, for events 2 and 3, the initial energies and positions of test ions are selected from Figures 5f, 5j, 6d, and 6h. We assume the initial value of α to be 175° (for events 1 and 2) or 5° (for event 3), because the Arase observations show the almost field-aligned distributions of H^+ and O^+ ions (Figures 3g, 3k, 5g, 5k, 6g, and 6k). Results of the calculation are displayed in Figure 11. We plot only the locations of the test ions at $t_{travel} = 0$ h, 2 h, 4 h, 6 h, 8 h, and 10 h, because drawing of all ion trajectories makes figures too complicated. Ions which are lost in the ionosphere or continue to travel for 10 h are denoted with open or closed circles, respectively. From Figures 11a–11d, we note that in event 1, after H^+ and O^+ ions are observed by Arase at premidnight (MLT ~ 23 h) and above the equator (GMLAT = 22°–23°), most of them drift eastward, travel through the dawn sector, and reach around noon

(MLT ~ 11 h) in 10 h. Ions are distributed along the geomagnetic field lines at $L \sim 5$ and are expected to have a bidirectional or normal distribution. In event 2 (Figures 11e–11h), both H^+ and O^+ ions start from more duskward (MLT ~ 21 h) above the equator, resulting in arrival at dawn along the geomagnetic field lines at $L \sim 4$ after the 10 h travel. Similar results are obtained for event 3 as indicated in Figures 11i–11l, although ions started from the southern inner magnetosphere (GMLAT ~ −17°).

6. Discussion

6.1. Comparison With Van Allen Probes Observations

From the 14-month data set of Arase/MGF and LEPi, we find 55 events of the low-energy O^+ flux enhancements accompanied with the magnetic field dipolarization. We perform both the case study and the statistical study, and find that the low-energy O^+ flux enhancements (a) start a few minutes after the dipolarization onset, (b) have energy-dispersed signatures with decreasing energy from a few keV down to ~10 eV, (c) have a field-aligned distribution ($\alpha \sim 0°$ below the equator and $\alpha \sim 180°$ above the equator), (d) occur in both storm and non-storm periods, (e) are accompanied by the low-energy H^+ flux enhancements that have lower energies than O^+ by a factor of 3–10, and (f) increase the O^+ density and the O^+/H^+ density ratio by ~10 times and 4–5 times on average, respectively.

Results 1, 2, and 3 are consistent with those reported by previous studies using the Van Allen Probes data (Chaston et al., 2015; Gkioulidou et al., 2019; Hull et al., 2019; Kistler et al., 2016; Nosé et al., 2016), indicating that these are common features of the low-energy O^+ flux enhancements. Although the previous studies reported only the flux enhancement events found during large magnetic storms, result 4 shows that the occurrence of them does not strongly depend on the geomagnetic activity.

For the June 1, 2013 event observed by Van Allen Probe A, the energy difference between H^+ and O^+ was described by Chaston et al. (2015) that the field-aligned O^+ flux enhancements are observed to extend to energies larger than found for H^+, although the degree of the flux difference was not examined. There were also a few studies that reported the energy difference above ~4,000 km altitude. Using data from the polar-orbiting S3-3 and DE-1 satellites, Collin et al. (1981, 1987) found that the average energy of upflowing O^+ is ~1.7 times higher than that of upflowing H^+. Möbius et al. (1998) showed the peak energy of upflowing O^+ ion beams is 1.5–4 times higher than that of H^+ ion beams from the FAST satellite measurements. Result 5 is qualitatively consistent with these previous results, although it is still controversial what mechanisms cause this energy difference. The mechanisms are considered to take effects when O^+ and H^+ ions are extracted from the ionosphere to the magnetosphere, and include not only acceleration by parallel electric field but also additional mass-dependent acceleration or energy transfer process between ions. Chaston et al. (2004, 2015, 2016) and Hull et al. (2019, 2020) proposed acceleration of O^+ ions by dispersive Alfvén waves. Collin et al. (1987) and Möbius et al. (1998) supposed ion beam instabilities for the energy transfer process. Shen and Knudsen (2020) argued that the most effective ion heating mechanism for O^+ ions is acceleration by short-scale electromagnetic ion cyclotron waves.

Variations of the ion density and the ion density ratio for the June 23, 2015 event were reported by Gkioulidou et al. (2019), who used ion flux data in the energy range of 30 eV–50 keV measured with the HOPE instrument onboard Van Allen Probe B. They found an increase of the O^+ density and its dominance (i.e., $O^+/H^+ = 1$–10) at $L < 5.8$. For event 1–3 observed by Arase, the O^+/H^+ density ratio is increased to 0.05–0.2, which is smaller than those by Van Allen Probe B. We think that the peak values of the O^+/H^+ density ratio depend on events. Result 6 statistically confirms the relative increase of the O^+ density to the H^+ density and indicates a possible contribution of the low-energy O^+ flux enhancements to the ion composition change in the inner magnetosphere.

6.2. Occurrence Probability of Low-Energy O^+ Flux Enhancements

According to the present analysis using the Arase data, the occurrence probability of the low-energy O^+ flux enhancements is 36% (=55/153). This number is smaller than that found from the Van Allen Probes data by Nosé et al. (2016), that is, 80% (=59/74). This would be because our data set covers the solar minimum period from April 2017 to January 2019, in which the F10.7 index is 60–70 solar flux unit (sfu, 1 sfu = 10^{-22} W/

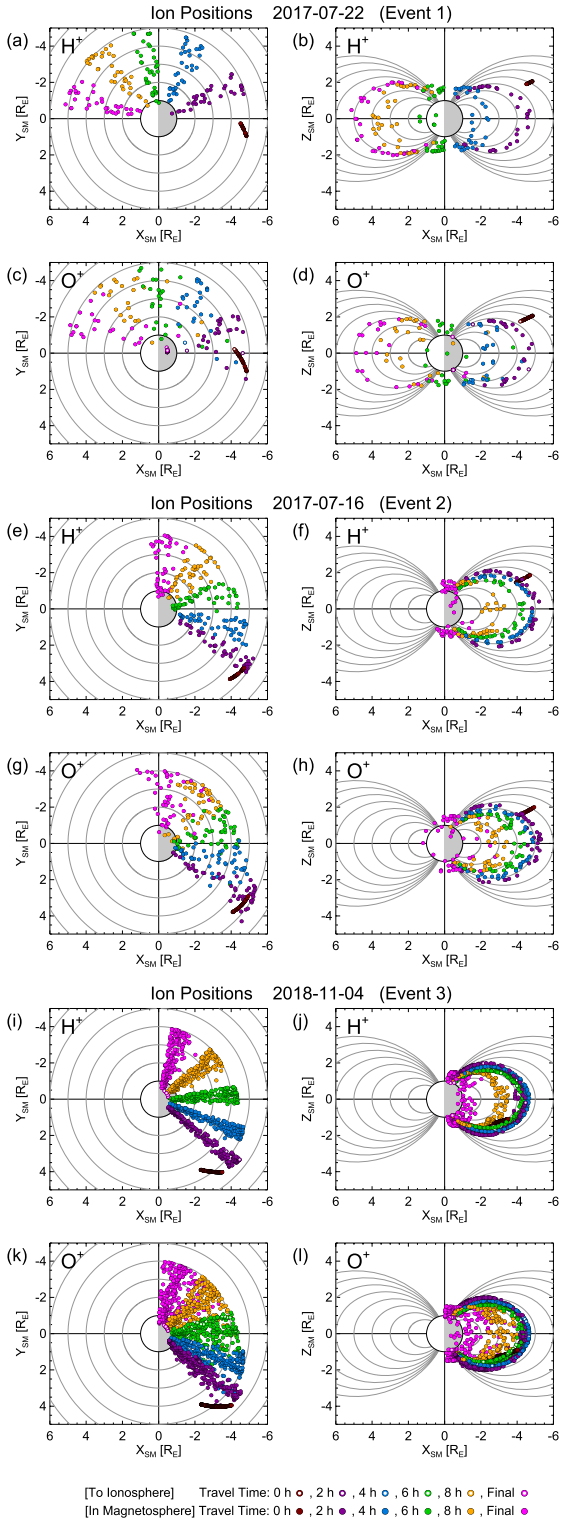

Figure 11. Numerical simulation results of positions of H^+ and O^+ ions that start from the Arase location with the observed energies for (a–d) event 1 (e–h) event 2, and (i–l) event 3. Ion positions are projected onto (left column) the geomagnetic equatorial plane and (right column) the geomagnetic noon-midnight meridional plane. The initial pitch angle is assumed to be 175° for events 1 and 2, and 5° for event 3. The same pitch angle scattering effect as Figures 10d–10f is included in the calculation. The ion position at a specific travel time is indicated with a circle with different colors as shown in the bottom of figure. Open or closed circles mean that the ion is finally lost in the ionosphere or survives in the magnetosphere for 10 h.

m^2/Hz), while the data set used by Nosé et al. (2016) spans the solar maximum period from October 2012 until October 2013, when the F10.7 index is approximately 100–150 sfu. It is expected that the low-energy O^+ ions observed by Arase and Van Allen Probes originate from the ionosphere and are extracted promptly at substorm onset. The occurrence frequency of upflowing O^+ ions at the high altitude of 8,000–23,000 km increases at the solar maximum (e.g., Yau et al., 1985, 1986). Therefore, during the solar maximum, the source region of ionospheric O^+ ions is shifted upwards and the ions somehow escape more easily from the ionosphere, resulting in the higher occurrence probability of the low-energy O^+ flux enhancements in the inner magnetosphere.

6.3. Possible Link to Warm Plasma Cloak and Oxygen Torus

Chappell et al. (2008) compiled data from multiple satellites and revealed the magnetospheric plasma populations that have energies of a few eV to greater than 400 eV and bidirectional field-aligned distribution. These populations are found just outside the plasmapause from the nightside to dawn, and extend from the plasmapause to the magnetopause on the dayside, being named "warm plasma cloak." Using data from the THEMIS satellite, Lee and Angelopoulos (2014) found that cold O^+ ions on the nightside have a temperature near hundreds of eV and warp around the dawn. These O^+ ions are consistent with the description of the warm plasma cloak by Chappell et al. (2008). The spatial distribution and the pitch angle distribution of the warm plasma cloak (i.e., from the nightside, via dawn, to the morning side, and bidirectional distribution) are quite consistent with the numerical simulation results shown in Figure 11. Arase observes O^+ ion enhancements in the energy range from ∼10 eV to a few keV, which is slightly higher than that of the warm plasma cloak (a few eV to >400 eV), but these energy ranges overlap each other. We, therefore, suppose that the low-energy O^+ flux enhancements can be a source of the warm plasma cloak.

It is noted that the oxygen torus is also discovered in the similar MLT range from the midnight to dawn and morning (Nosé, Matsuoka, Kumamoto, et al., 2018, 2020; Roberts et al., 1987). Gkioulidou et al. (2019) concluded that the low-energy O^+ flux enhancements observed by Van Allen Probes can contribute to the formation of the oxygen torus. However, the oxygen torus is expected to be composed of thermal ions with energies less than ∼50 eV (Chappell, 1982; Comfort et al., 1988; Horwitz et al. 1984, 1986, 1990). Thus, only a small portion of the low-energy O^+ flux enhancements in the lowest energies (∼10 eV) can be a source of oxygen torus.

6.4. Choice of Model Fields in Numerical Simulation

In the above numerical simulation, we use Kp = 2 for the T89 magnetic model field and the Volland-Stern electric model field. This Kp value is appropriate for non-storm periods. However, the Kp index becomes larger during the storm recovery phase or main phase; thus, we conduct the similar numerical calculation with Kp = 4. It is revealed that trajectories of O^+ ions with three different energies are almost the same as Figure 10 for both cases with/without the pitch angle scattering effect, except that O^+ ions are transported further inward because of the stronger convention electric field. Regarding the forward tracing of ion trajectories from the Arase position, in event 1, the result with Kp = 4 is found to be similar to that with Kp = 2 (Figures 11a–11d). In event 2 and 3, however, the result with Kp = 4 becomes quite different from that with Kp = 2 (Figures 11e–11l), where both H^+ and O^+ ions drift eastward and sunward, and finally hit the magnetopause. This is because the convection drift velocity (sunward) is larger than the corotation drift velocity (westward) when Kp = 4, and ions starting from the premidnight sector (MLT = 20–22 h) move sunward, traverse the duskside magnetosphere, and reach the magnetopause. It is supposed that the convection electric field plays an essential role in controlling trajectories of low-energy ions (<a few keV). Thus, in future study, it is important to use a more realistic convection electric field model in the inner magnetosphere such as the UNH-IMEF model (Matsui et al., 2004, 2008).

The magnetic field model used in the present calculation does not change in time, which is different from the Arase observations (Figures 3c, 5c, and 6c). It may be possible to use more recent magnetic field models that use the solar wind parameters as inputs. They provide temporal variations of the magnetic field, but do not derive the induced electric field, which could energize/deenergize ions. Therefore, if the temporal variations of the magnetic field should be considered in the numerical calculation, it is better to use results from self-consistent inner magnetospheric models.

7. Conclusions

In this study, we have investigated the low-energy O^+ flux variations observed by the Arase satellite in the inner magnetosphere (MLT = 18–04 h and L = 4.0–8.0) in the periods of April 1–October 31, 2017 and July 1, 2018–January 31, 2019. After a few minutes of the magnetic dipolarization, the O^+ flux enhancements appear with a clear energy-dispersed signature decreasing from a few keV to ~10 eV. They have a field-aligned pitch angle distribution in the parallel or antiparallel direction, when Arase is located below or above the geomagnetic equator, respectively. The field-aligned low-energy O^+ flux enhancements are accompanied by the similar H^+ flux enhancements, although the H^+ peak energy is approximately 3–10 times lower than the O^+ peak energy. These results are consistent with those reported by previous studies employing Van Allen Probes.

In order to examine the effect of the low-energy ion flux enhancements on the inner magnetosphere, we perform a numerical simulation in which ion trajectories are traced forward in time from the Arase positions. It is found that both H^+ and O^+ ions drift eastward and reach the dawn-to-morning sector in 10 h without being lost in the ionosphere, if the small pitch angle scattering process ($\Delta\alpha = 5°$) is included even only in the first equatorial crossing. The numerical simulation results lead us to suppose that the low-energy ion flux enhancements can be a source of the warm plasma cloak (or the oxygen torus partly), because their spatial distribution, the pitch angle distribution, and the energy range of ions are very similar to each other. The Arase observations show that the O^+ density and the O^+/H^+ density ratio are increased by ~10 times and 4–5 times, respectively, in association with the low-energy ion flux enhancements. We therefore suppose that the low-energy ion flux enhancements cause the ion composition change of the warm plasma cloak, that is, O^+-rich warm plasma cloak. According to the Arase measurements, there is no clear dependence on geomagnetic condition in occurrence of the field-aligned low-energy O^+ flux enhancements. Thus, the warm plasma cloak (or possibly the oxygen torus) is considered to be formed even during quiet intervals.

Data Availability Statement

Science data of the ERG (Arase) satellite were obtained from the ERG Science Center (Miyoshi, Hori, et al., 2018) operated by ISAS/JAXA and ISEE/Nagoya University (https://ergsc.isee.nagoya-u.ac.jp/index.shtml.en). The present study analyzed the ORB L2_v03 data, the MGF L2_ v03.04 data, and the LEPi L2_v03.00 data. The AE index is provided by the World Data Center for Geomagnetism, Kyoto, and is available at https://doi.org/10.17593/15031-54800. The Wp index is available at https://doi.org/10.17593/13437-46800. The Kp index was provided by J. Matzka at the Helmholtz Center Potsdam, GFZ German Research Center for Geosciences, and is available at https://doi.org/10.5880/Kp.0001. Geomagnetic field by the IGRF-13 and T89 models was calculated with GEOPACK routines developed by N. A. Tsyganenko and coded by H. Korth. The numerical simulation code for ion trajectories was provided by D. C. Delcourt. We acknowledge use of NASA/GSFC's Space Physics Data Facility's OMNIWeb service and OMNI data (https://omniweb.gsfc.nasa.gov/).

Acknowledgments
This study is supported by the Japan Society for the Promotion of Science (JSPS), grant-in-aid for scientific research (B) (grant 16H04057 and 21H01147), challenging research (pioneering) (grant 17K18804), and grant-in-aid for specially promoted research (grant 16H06286); as well as Ito Kagaku Shinkou Kai and Yamada Kagaku Shinkou Zaidan. Y. Miyoshi is supported by the Japan Society for the Promotion of Science (JSPS), grant-in-aid for scientific research on innovative areas (grant 15H05815) and grant-in-aid for scientific research (B) (grant 20H01959).

References

Alken, P., Erwan, T., Beggan, C. D., Amit, H., Aubert, J., Baerenzung, J., et al. (2021). International geomagnetic reference field: The thirteenth generation. *Earth Planets and Space*, *73*(1). https://doi.org/10.1186/s40623-020-01281-4

Asamura, K., Kazama, Y., Yokota, S., Kasahara, S., & Miyoshi, Y. (2018). Low-energy particle experiments–ion mass analyzer (LEPi) onboard the ERG (Arase) satellite. *Earth Planets and Space*, *70*, 70. https://doi.org/10.1186/s40623-018-0846-0

Asamura, K., Miyoshi, Y., & Shinohara, I. (2018). The LEPi instrument Level-2 3D flux data of Exploration of energization and Radiation in Geospace (ERG) Arase satellite, Version v03.00. ERG Science Center, Institute for Space-Earth Environmental Research, Nagoya University. https://doi.org/10.34515/DATA.ERG-05000

Chappell, C. R. (1982). Initial observations of thermal plasma composition and energetics from Dynamics Explorer-1. *Geophysical Research Letters*, *9*(9), 929–932. https://doi.org/10.1029/GL009i009p00929

Chappell, C. R., Huddleston, M. M., Moore, T. E., Giles, B. L., & Delcourt, D. C. (2008). Observations of the warm plasma cloak and an explanation of its formation in the magnetosphere. *Journal of Geophysical Research*, *113*, A09206. https://doi.org/10.1029/2007JA012945

Chaston, C. C., Bonnell, J. B., Carlson, C. W., McFadden, J. P., Ergun, R. E., & Lund, E. J. (2004). Auroral ion acceleration in dispersive Alfvén waves. *Journal of Geophysical Research*, *109*, A04205. https://doi.org/10.1029/2003JA010053

Chaston, C. C., Bonnell, J. W., Reeves, G. D., & Skoug, R. M. (2016). Driving ionospheric outflows and magnetospheric O^+ energy density with Alfvén waves. *Geophysical Research Letters*, *43*, 4825–4833. https://doi.org/10.1002/2016GL069008

Chaston, C. C., Bonnell, J. W., Wygant, J. R., Kletzing, C. A., Reeves, G. D., Gerrard, A., et al. (2015). Extreme ionospheric ion energization and electron heating in Alfvén waves in the storm time inner magnetosphere. *Geophysical Research Letters*, *42*, 10531–10540. https://doi.org/10.1002/2015GL066674

Collin, H. L., Peterson, W. K., & Shelley, E. G. (1987). Solar cycle variation of some mass dependent characteristics of upflowing beams of terrestrial ions. *Journal of Geophysical Research*, *92*(A5), 4757–4762. https://doi.org/10.1029/JA092iA05p04757

Collin, H. L., Sharp, R. D., Shelley, E. G., & Johnson, R. G. (1981). Some general characteristics of upflowing ion beams over the auroral zone and their relationship to auroral electrons. *Journal of Geophysical Research*, *86*(A8), 6820–6826. https://doi.org/10.1029/JA086iA08p06820

Comfort, R. H. (1996). Thermal structure of the plasmasphere. *Advances in Space Research*, *17*, 175–184. https://doi.org/10.1016/0273-1177(95)00710-V

Comfort, R. H., Newberry, I. T., & Chappell, C. R. (1988). Preliminary statistical survey of plasmaspheric ion properties from observations by DE 1/RIMS. In T. E. Moore, J. H. Waite, T. W. Moorehead, & W. B. Hanson (Eds.), *Modeling magnetospheric plasma. Geophysical Monograph Series* (Vol. 44, pp. 107–114). Washington, DC. American Geophysical Union. https://doi.org/10.1029/GM044p0107

Craven, P. D., Comfort, R. H., Gallagher, D. L., & West, R. (1991). A study of the statistical behavior of ion temperatures from DE 1/RIMS. In G. R. Wilson (Ed.), *Modeling magnetospheric plasma processes. Geophysical Monograph Series* (Vol. 62, pp. 173–182). Washington, DC. American Geophysical Union. https://doi.org/10.1029/GM062p0173

Delcourt, D. C., Sauvaud, J. A., & Pedersen, A. (1990). Dynamics of single-particle orbits during substorm expansion phase. *Journal of Geophysical Research*, *95*(A12), 20853–20865. https://doi.org/10.1029/JA095iA12p20853

Gkioulidou, M., Ohtani, S., Ukhorskiy, A. Y., Mitchell, D. G., Takahashi, K., Spence, H. E., et al. (2019). Low-energy (<keV) O^+ ion outflow directly into the inner magnetosphere: Van Allen Probes observations. *Journal of Geophysical Research: Space Physics*, *124*, 405–419. https://doi.org/10.1029/2018JA025862

Horwitz, J. L., Comfort, R. H., Brace, L. H., & Chappell, C. R. (1986). Dual-spacecraft measurements of plasmasphere-ionosphere coupling. *Journal of Geophysical Research*, *91*(A10), 11203–11216. https://doi.org/10.1029/JA091iA10p11203

Horwitz, J. L., Comfort, R. H., & Chappell, C. R. (1984). Thermal ion composition measurements of the formation of the new outer plasmasphere and double plasmapause during storm recovery phase. *Geophysical Research Letters*, *11*(8), 701–704. https://doi.org/10.1029/GL011i008p00701

Horwitz, J. L., Comfort, R. H., Richards, P. G., Chandler, M. O., Chappell, C. R., Anderson, P., et al. (1990). Plasmasphere-ionosphere coupling 2: Ion composition measurements at plasmaspheric and ionospheric altitudes and comparison with modeling results. *Journal of Geophysical Research*, *95*(A6), 7949–7959. https://doi.org/10.1029/JA095iA06p07949

Hull, A. J., Chaston, C. C., Bonnell, J. W., Damiano, P. A., Wygant, J. R., & Reeves, G. D. (2020). Correlations between dispersive Alfvén wave activity, electron energization, and ion outflow in the inner magnetosphere. *Geophysical Research Letters*, *47*, e2020GL088985. https://doi.org/10.1029/2020GL088985

Hull, A. J., Chaston, C. C., Bonnell, J. W., Wygant, J. R., Kletzing, C. A., Reeves, G. D., & Gerrard, A. (2019). Dispersive Alfvén wave control of O^+ ion outflow and energy densities in the inner magnetosphere. *Geophysical Research Letters*, *46*, 8597–8606. https://doi.org/10.1029/2019GL083808

Kistler, L. M., Mouikis, C. G., Spence, H. E., Menz, A. M., Skoug, R. M., Funsten, H. O., et al. (2016). The source of O^+ in the storm time ring current. *Journal of Geophysical Research: Space Physics*, *121*, 5333–5349. https://doi.org/10.1002/2015JA022204

Kokubun, S., & McPherron, R. L. (1981). Substorm signatures at synchronous altitude. *Journal of Geophysical Research*, *86*(A13), 11265–11277. https://doi.org/10.1029/JA086iA13p11265

Kumamoto, A., Tsuchiya, F., Kasahara, Y., Kasaba, Y., Kojima, H., Yagitani, S., et al. (2018). High frequency analyzer (HFA) of plasma wave experiment (PWE) onboard the Arase spacecraft. *Earth, Planets and Space*, *70*(1), 82. https://doi.org/10.1186/s40623-018-0854-0

Lee, J. H., & Angelopoulos, V. (2014). On the presence and properties of cold ions near Earth's equatorial magnetosphere. *Journal of Geophysical Research: Space Physics*, *119*, 1749–1770. https://doi.org/10.1002/2013JA019305

Lennartsson, W. (1989). Energetic (0.1- to 16-keV/e) magnetospheric ion composition at different levels of solar F10.7. *Journal of Geophysical Research*, *94*(A4), 3600–3610. https://doi.org/10.1029/JA094iA04p03600

Lopez, R. E., Lui, A. T. Y., Sibeck, D. G., McEntire, R. W., Zanetti, L. J., Potemra, T. A., & Krimigis, S. M. (1988). The longitudinal and radial distribution of magnetic reconfigurations in the near-Earth magnetotail as observed by AMPTE/CCE. *Journal of Geophysical Research*, *93*, 997–1001. https://doi.org/10.1029/JA093iA02p00997

Lui, A. T. Y., & Najmi, A.-H. (1997). Time-frequency decomposition of signals in a current disruption event. *Geophysical Research Letters*, *24*, 3157–3160. https://doi.org/10.1029/97GL03229

Lui, A. T. Y., Yoon, P. H., Mok, C., & Ryu, C.-M. (2008). Inverse cascade feature in current disruption. *Journal of Geophysical Research*, *113*, A00C06. https://doi.org/10.1029/2008JA013521

Matsui, H., Jordanova, V. K., Quinn, J. M., Torbert, R. B., & Paschmann, G. (2004). Derivation of electric potential patterns in the inner magnetosphere from Cluster EDI data: Initial results. *Journal of Geophysical Research*, *109*, A10202. https://doi.org/10.1029/2003JA010319

Matsui, H., Puhl-Quinn, P. A., Jordanova, V. K., Khotyaintsev, Y., Lindqvist, P.-A., & Torbert, R. B. (2008). Derivation of inner magnetospheric electric field (UNH-IMEF) model using Cluster data set. *Annales Geophysicae*, *26*, 2887–2898. https://doi.org/10.5194/angeo-26-2887-2008

Matsuoka, A., Teramoto, M., Imajo, S., Kurita, S., Miyoshi, Y., & Shinohara, I. (2018). The MGF instrument Level-2 spin-fit magnetic field data of Exploration of energization and Radiation in Geospace (ERG) Arase satellite, Version v03.04. ERG Science Center, Institute for Space-Earth Environmental Research, Nagoya University. https://doi.org/10.34515/DATA.ERG-06001

Matsuoka, A., Teramoto, M., Nomura, R., Nosé, M., Fujimoto, A., Tanaka, Y., et al. (2018). The Arase (ERG) magnetic field investigation. *Earth Planets and Space*, *70*, 43. https://doi.org/10.1186/s40623-018-0800-1

Matzka, J., Bronkalla, O., Tornow, K., Elger, K., & Stolle, C. (2021). Geomagnetic Kp index. V. 1.0. GFZ Data Services. https://doi.org/10.5880/Kp.0001

Maynard, N. C., & Chen, A. J. (1975). Isolated cold plasma regions—Observations and their relation to possible production mechanisms. *Journal of Geophysical Research*, *80*, 1009–1013. https://doi.org/10.1029/JA080i007p01009

Miyoshi, Y., Hori, T., Shoji, M., Teramoto, M., Chang, T.-F., Segawa, T., et al. (2018). The ERG Science Center. *Earth Planets and Space*, *70*, 96. https://doi.org/10.1186/s40623-018-0867-8

Miyoshi, Y., Shinohara, I., & Jun, C.-W. (2018). The Level-2 orbit data of Exploration of energization and Radiation in Geospace (ERG) Arase satellite, Version v03. ERG Science Center, Institute for Space-Earth Environmental Research, Nagoya University. https://doi.org/10.34515/DATA.ERG-12000

Miyoshi, Y., Shinohara, I., Takashima, T., Asamura, K., Higashio, N., Mitani, T., et al. (2018). Geospace Exploration Project ERG. *Earth Planets and Space*, *70*, 101. https://doi.org/10.1186/s40623-018-0862-0

Möbius, E., Tang, L., Kistler, L. M., Popecki, M., Lund, E. J., Klumpar, D., et al. (1998). Species dependent energies in upward directed ion beams over auroral arcs as observed with FAST TEAMS. *Geophysical Research Letters*, *25*, 2029–2032. https://doi.org/10.1029/98GL00381

Nagai, T. (1982). Observed magnetic substorm signatures at synchronous altitude. *Journal of Geophysical Research*, *87*(A6), 4405–4417. https://doi.org/10.1029/JA087iA06p04405

Nosé, M., Iyemori, T., Wang, L., Hitchman, A., Matzka, J., Feller, M., et al. (2012). Wp index: A new substorm index derived from high-resolution geomagnetic field data at low latitude. *Space Weather*, *10*, S08002. https://doi.org/10.1029/2012SW000785

Nosé, M., Keika, K., Kletzing, C. A., Spence, H. E., Smith, C. W., MacDowall, R. J., et al. (2016). Van Allen Probes observations of magnetic field dipolarization and its associated O^+ flux variations in the inner magnetosphere at $L < 6.6$. *Journal of Geophysical Research: Space Physics*, *121*, 7572–7589. https://doi.org/10.1002/2016JA022549

Nosé, M., Koshiishi, H., Matsumoto, H., C:son Brandt, P., Keika, K., Koga, K., et al. (2010). Magnetic field dipolarization in the deep inner magnetosphere and its role in development of O^+-rich ring current. *Journal of Geophysical Research*, *115*, A00J03. https://doi.org/10.1029/2010JA015321

Nosé, M., Matsuoka, A., Kasahara, S., Yokota, S., Teramoto, M., Keika, K., et al. (2018). Magnetic field dipolarization and its associated ion flux variations in the dawnside deep inner magnetosphere: Arase observations. *Geophysical Research Letters*, *45*, 7942–7950. https://doi.org/10.1029/2018GL078825

Nosé, M., Matsuoka, A., Kumamoto, A., Kasahara, Y., Goldstein, J., Teramoto, M., et al. (2018). Longitudinal structure of oxygen torus in the inner magnetosphere: Simultaneous observations by Arase and Van Allen Probe A. *Geophysical Research Letters*, *45*, 177–210. https://doi.org/10.1029/2018GL080122

Nosé, M., Matsuoka, A., Kumamoto, A., Kasahara, Y., Teramoto, M., Kurita, S., et al. (2020). Oxygen torus and its coincidence with EMIC wave in the deep inner magnetosphere: Van Allen Probe B and Arase observations. *Earth Planets and Space*, *72*, 111. https://doi.org/10.1186/s40623-020-01235-w

Nosé, M., Takahashi, K., Keika, K., Kistler, L. M., Koga, K., Koshiishi, H., et al. (2014). Magnetic fluctuations embedded in dipolarization inside geosynchronous orbit and their associated selective acceleration of O^+ ions. *Journal of Geophysical Research: Space Physics*, *119*, 4639–4655. https://doi.org/10.1002/2014JA019806

Ohtani, S., Creutzberg, F., Mukai, T., Singer, H., Lui, A. T. Y., Nakamura, M., et al. (1999). Substorm onset timing: The December 31, 1995, event. *Journal of Geophysical Research*, *104*(A10), 22713–22727. https://doi.org/10.1029/1999JA900209

Ohtani, S., Higuchi, T., Lui, A. T. Y., & Takahashi, K. (1995). Magnetic fluctuations associated with tail current disruption: Fractal analysis. *Journal of Geophysical Research*, *100*, 19135–19146. https://doi.org/10.1029/95JA00903

Ohtani, S., Takahashi, K., Higuchi, T., Lui, A. T. Y., Spence, H. E., & Fennell, J. F. (1998). AMPTE/CCE-SCATHA simultaneous observations of substorm-associated magnetic fluctuations. *Journal of Geophysical Research*, *103*, 4671–4682. https://doi.org/10.1029/97JA03239

Pulkkinen, T. I., Baker, D. N., Frank, L. A., Sigwarth, J. B., Opgenoorth, H. J., Greenwald, R., et al. (1998). Two substorm intensifications compared: Onset, expansion, and global consequences. *Journal of Geophysical Research*, *103*(A1), 15–27. https://doi.org/10.1029/97JA01985

Roberts, W. T., Jr., Horwitz, J. L., Comfort, R. H., Chappell, C. R., Waite, J. H., Jr., & Green, J. L. (1987). Heavy ion density enhancements in the outer plasmasphere. *Journal of Geophysical Research*, *92*(A12), 13499–13512. https://doi.org/10.1029/JA092iA12p13499

Shen, Y., & Knudsen, D. J. (2020). On O^+ ion heating by BBELF waves at low altitude: Test particle simulations. *Journal of Geophysical Research: Space Physics*, *125*, e2019JA027291. https://doi.org/10.1029/2019JA027291

Stern, D. P. (1975). The motion of a proton in the equatorial magnetosphere. *Journal of Geophysical Research*, *80*, 595–599. https://doi.org/10.1029/JA080i004p00595

Tsyganenko, N. A. (1989). A magnetospheric magnetic field model with a warped tail current sheet. *Planetary and Space Science*, *37*, 5–20. https://doi.org/10.1016/0032-0633(89)90066-4

Volland, H. (1973). A semiempirical model of large-scale magnetospheric electric fields. *Journal of Geophysical Research*, *78*, 171–180. https://doi.org/10.1029/JA078i001p00171

World Data Center for Geomagnetism, Kyoto, & Nosé, M. (2016). Geomagnetic Wp index. https://doi.org/10.17593/13437-46800

World Data Center for Geomagnetism, Kyoto, Nosé, M., Iyemori, T., Sugiura, M., & Kamei, T. (2015). Geomagnetic AE index. https://doi.org/10.17593/15031-54800

Yau, A. W., Beckwith, P. H., Peterson, W. K., & Shelley, E. G. (1985). Long-term (solar cycle) and seasonal variations of upflowing ionospheric ion events at DE 1 altitudes. *Journal of Geophysical Research*, *90*(A7), 6395–6407. https://doi.org/10.1029/JA090iA07p06395

Yau, A. W., Shelley, E. G., & Peterson, W. K. (1986). Accelerated auroral and polar-cap ions: Outflow at DE-1 altitudes. In T. Chang, M. K. Hudson, J. R. Jasperse, R. G. Johnson, P. M. Kintner, & M. Schulz (Eds.), *Ion acceleration in the magnetosphere and ionosphere, Geophysical Monograph Series* (Vol. 38, pp. 72–76). Washington, DC. American Geophysical Union. https://doi.org/10.1029/GM038p0072